ARTICLE

Check for updates

Aqueous alteration of the Vastitas Borealis Formation at the Tianwen-1 landing site

Changqing Liu[1], Zongcheng Ling [1,2 ✉], Zhongchen Wu[1], Jiang Zhang[1], Jian Chen [1], Xiaohui Fu [1], Le Qiao [1], Ping Liu[1], Bo Li[1], Li Zhang[3], Yanqing Xin[1], Erbin Shi[1], Haijun Cao[1], Shangke Tian[1], Sheng Wan[1], Hongchun Bai[1] & Jianzhong Liu [4]

The Vastitas Borealis Formation is a Hesperian-aged sedimentary unit that mainly covers the Martian northern plains. Its environment of formation is uncertain but may be related to an ancient Martian ocean, outflow channel deposits, compaction and drainage activities, or subsurface ice-related processes. Here we investigate the geological evolution of the Vastitas Borealis Formation using geochemical and mineralogical data acquired by the Mars Surface Composition Detector on board the Zhurong rover at the Tianwen-1 landing site. We find that the fine-grained soil is very similar to the ubiquitous surface dust at other landing sites on Mars but mixed with calcium-rich and magnesium-poor local materials. These materials are mostly igneous minerals mixed with allophane and imogolite/opal and appear to have a low degree of chemical alteration. We suggest that these deposits likely formed by alteration of extensive volcaniclastic soils in limited or ephemeral water under cold conditions, which largely supports the hypotheses of a frozen ocean and sublimation.

[1] Shandong Key Laboratory of Optical Astronomy and Solar-Terrestrial Environment, School of Space Science and Physics, Institute of Space Sciences, Shandong University, 264209 Weihai, China. [2] CAS Center for Excellence in Comparative Planetology, Chinese Academy of Sciences, 230026 Hefei, China. [3] School of Mechanical, Electrical and Information Engineering, Shandong University, 264209 Weihai, China. [4] Institute of Geochemistry, Chinese Academy of Sciences, 550002 Guiyang, China. ✉email: zcling@sdu.edu.cn

China's first Mars exploration mission Tianwen-1 has landed and released the Zhurong (ZR) rover in southern Utopia Planitia on the northern hemisphere of Mars on 15 May 2021[1–4], within the Late Hesperian-aged geologic unit named the Vastitas Borealis Formation (VBF)[1,4–6]. The VBF is one of the most widespread sedimentary units on Mars that covers most of the northern plains (Fig. 1a)[7–9]. The boundary of the VBF resembles closely the shoreline of a potential ancient ocean due to the cliffs separating the uplands and plains[10–12]. Several fretted terrains within VBF including curvilinear ridges and stepped massifs with terraced slopes are also proposed to be related to the potential ocean[10–12]. Moreover, VBF has kilometer-scale surface roughness relevant to a non-volcanic origin[10]. Based on those observations, several previous studies proposed that the VBF material is a sedimentary deposit from a standing body of water that might be an Upper Hesperian ocean[6,10–13].
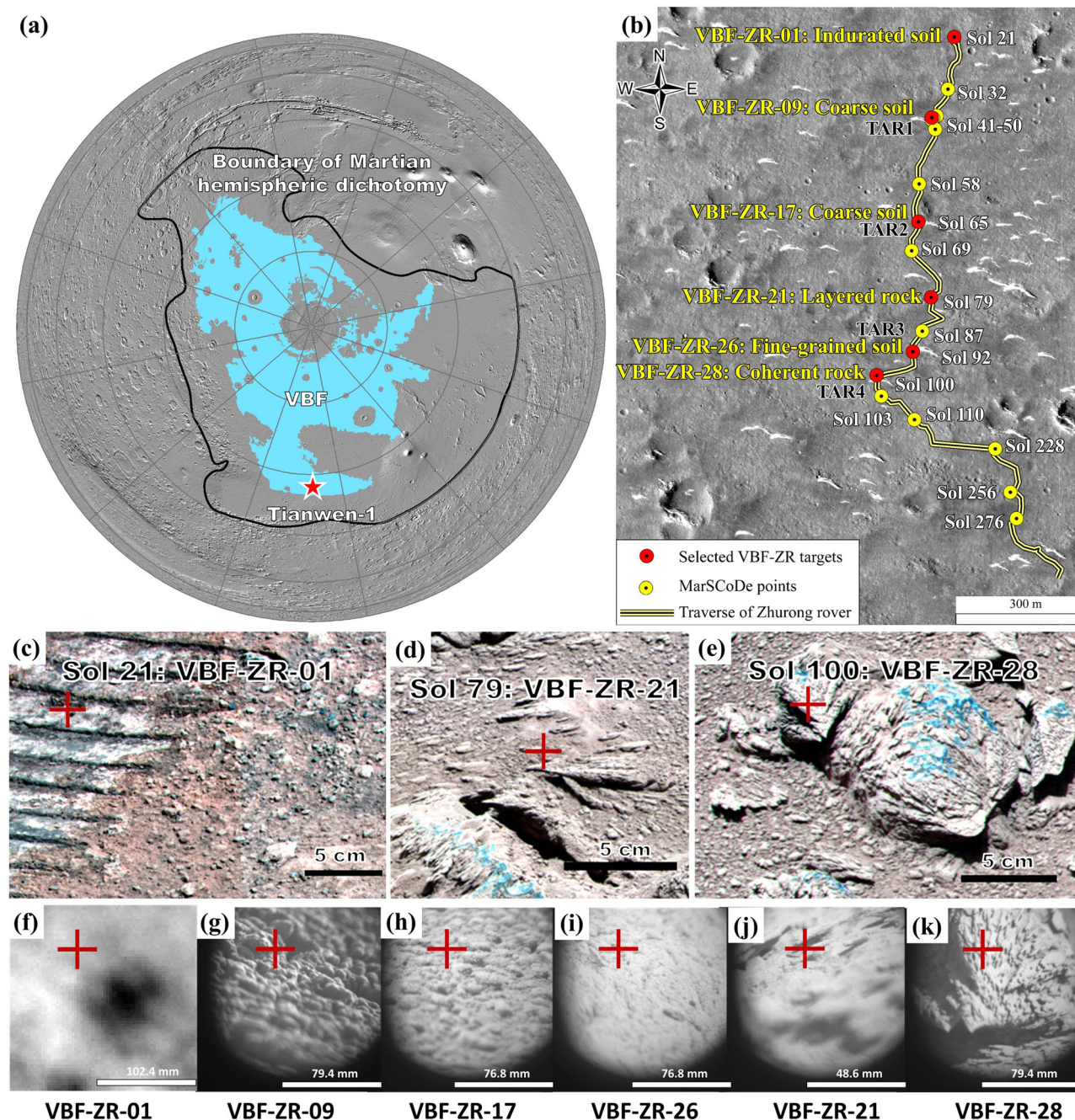

Fig. 1 Landing site, traverse map, and MI images of six VBF-ZR targets. a Distribution map of the VBF unit on the Northern Plains of Mars. The map base is a Mars Orbiter Laser Altimeter (MOLA) shaded-relief image. b Traverse map of the ZR rover up to sol 300 overlain on the base image of High-Resolution Imaging Camera (HiRIC) data. The HiRIC raw data is provided by China National Space Administration. The yellow points represent the locations of MarSCoDe targets, and the red points indicate the locations of six VBF-ZR targets discussed in this study. c–e The images of VBF-ZR-01, VBF-ZR-21, and VBF-ZR-28 targets collected by the Multispectral Camera (R 650 nm, G 525 nm, B 480 nm). f The MI images of VBF-ZR-01 target (the first target detected at the landing site, 64 × 64 pixels), g, h coarse-grained soils (VBF-ZR-09 at TAR1, VBF-ZR-17 at TAR2, 1024 × 1024 pixels), i fine-grained soils (VBF-ZR-26 at TAR3, 1024 × 1024 pixels), j a layered rock (VBF-ZR-21, 1024 × 1024 pixels), and k a coherent rock (VBF-ZR-28 at TAR4, 1024 × 1024 pixels). In these MI images, the red cross indicates the laser-ablated crater.

A circumpolar ocean was also proposed based on a coupled model with a dynamic ocean and atmosphere[14]. In addition, the pebbles, cobbles, and boulders in VBF may be deposited by a catastrophic flood[15], suggesting that the VBF has flood deposits from outflow channels[5,16]. However, the polygonal cracking, potential mud volcanoes, and viscous flow features within the VBF also suggest a hypothesis that VBF materials may be the compaction and drainage of a fluid-laden sedimentary unit[17,18]. In addition, several geological ice-related features are distributed across the VBF including pancake-like ejecta, rampart craters, pitted-wall craters, giant polygonal troughs, and concentric crater fill, which are interpreted to represent an energetic release of volatiles and sublimation of ice-layer from subsurface[1,4,19]. Moreover, the craters with low depth/diameter ratios and potential mud volcanos in the VBF also suggest a substantial amount of ground ice[4,20], consistent with the inferred subsurface water/ice in Utopia Planitia from shallow radar detections[21]. In summary, direct evidence of the origin of the VBF is still unclear based on available mission data.

VBF materials are geological indicators of the VBF origin. It was hypothesized that the chemical compositions at Viking 1 and Pathfinder landing sites are representative of the average compositions of the VBF[22]. The soils at these landing sites are rich in S and Cl elements[23,24], where the sulfate in soil crusts may be concentrated through intergranular leaching, upward transport, and intergranular evaporative precipitation[23]. Measurements from Viking 1 and Pathfinder landing sites were unable to provide enough information to constrain the origin of the VBF. The ZR rover landed at a new site in the VBF and has traversed over 1800 meters (Fig. 1b) in the first 300 sols, providing a unique opportunity to investigate the VBF materials. The ZR rover carries a Mars Surface Composition Detector (MarSCoDe) instrument suite, consisting of a Laser-Induced Breakdown Spectrometer (LIBS), a Short-Wave Infrared Spectrometer (SWIR), and a Micro-Imaging Camera (MI), with the intent to investigate the elemental compositions (Si, Al, Fe, Ca, Mg, K, Na, O, H, etc.), mineralogy, and morphology of encountered rocks and soils[25–27].

This study combined the analyses of LIBS and SWIR spectra from MarSCoDe to investigate the composition and mineralogy of VBF-ZR targets, with the intent to provide ground truth and further constraints for the origin of VBF, and evaluate whether the VBF could have been deposited by an ancient ocean.

Results and discussion
Six VBF-ZR targets and their geomorphology.
The terrain of ZR rover traverse is flat, covered by reddish soils and dust. Dark-toned materials are exposed in the surface with dust removed by the turbulent airflow and wheel track (Supplementary Fig. 1a, b), suggesting potential volcanic materials under the covered soils and dust. Four barchan-like Transverse Aeolian Ridges (TARs) are observed by the ZR rover (Fig. 1b). Those TARs have brighter albedo than the surrounding materials and intermittent distribution of dark and bright sand, suggesting that they are covered by dust and hence inactive and ancient[28,29]. During the first 300 sols, 38 targets have been measured by the LIBS and SWIR spectrometers (Supplementary Table 1), and several targets are near the TARs. This study selected six VBF-ZR targets along the traverse, including coarse and fine-grained soils and two types of rocks, to show their morphological, chemical and mineralogical characteristics (the data of all other VBF-ZR targets are presented in Supplementary Table 1, Supplementary Table 5, Supplementary Table 8, and included in the discussion). The first target (VBF-ZR-01, Fig. 1c, f) is an indurated soil with the surface dust removed by the exhaust plumes during the landing procedure and

indurated by wheel tracks. Two types of soils (coarse- and fine-grained) are observed near TARs, including two coarse-grained soils with a grain size of ~6 mm (VBF-ZR-09, Fig. 1g; VBF-ZR-17, Fig. 1h) and a fine-grained soil (VBF-ZR-26, Fig. 1i) with grains smaller than the resolution of MI (~150 μm per pixel, see Supplementary Notes 1). A layered rock (VBF-ZR-21, Fig. 1d, j) between TARs may be an outcrop with irregular layers that are probably related to wind erosion and subsequent deposition of fine-grained materials (e.g., dust). A coherent rock near TAR4 (VBF-ZR-28, Fig. 1e, k) displays channels and angular shapes that are probably caused by the long-termed erosion of wind. In addition, the undetected mineral grains in the layered rock and coherent rock may be less than the resolution of MI (~150 μm) or covered by a weathered (or dust-covered) surface.

Mineral identification by SWIR data analysis.
The visible and near-infrared spectra (Fig. 2) acquired by SWIR provide the mineralogy of VBF-ZR materials. After wavelength calibration (Supplementary Fig. 2 and Supplementary Table 2), the SWIR spectra are calibrated using two on-board SWIR calibration targets (white and gray pieces of cal-targets, Supplementary Fig. 3), and similar absorption features are observed (Supplementary Fig. 4). All spectra from the selected six VBF-ZR targets (Fig. 2) exhibit a deep iron-related broad absorption band near ~980 nm[30] and a negative slope from ~1600 nm to 2000 nm, which can be assigned to the absorption feature of pyroxene, similar to the Fe-rich orthopyroxene (OPX, $Wo_{2.5}En_{39}Fs_{58.5}$, No. C1DL14) and clinopyroxene spectra (CPX, $Wo_{42.6}En_7Fs_{50.4}$, No. C1DD148) from the Brown University Reflectance Experiment Laboratory (RELAB) database. The absorption center of VBF-ZR targets (~980 nm) is closer to the center of Ca-rich CPX ($Wo_{42.6}$, 1015 nm) compared to that of Ca-poor OPX ($Wo_{2.5}$, 939 nm), suggesting high-Ca pyroxene in these VBF-ZR targets. Several H_2O/OH absorption features appear in these SWIR spectra, including a broad band at ~2200 nm (OH combination stretching plus bending band[31]), ~1400 nm (H_2O stretching overtone band[31]), and ~1900 nm (H_2O combination stretching plus bending band[31]). These three bands are similarly found in the spectra of synthetic allophane (containing 5 wt.% Fe, No. C1JBA75), imogolite (No. C1JBA34), and opal (No. C1JBA33) in the RELAB spectral database. Especially the broad band at ~2227 nm is consistent with the poorly-crystalline phases (i.e., allophane and imogolite). While the band center of this feature is shorter than imogolite and opal (~2260 nm) and longer than allophane (~2202 nm), suggesting a mixture of allophane and imogolite/opal.

Note that SWIR spectra of VBF-ZR targets have triple features at ~1946 nm, ~2000 nm, and ~2040 nm, mainly contributed by the Martian atmosphere[32]. Therefore, the H_2O bands at ~1900 nm are weaker than laboratory spectra of hydrated aluminosilicates due to the potential masked features of the Martian atmosphere. In addition, the similarity of SWIR spectra along the ZR traverse should be caused by the mixture of local materials and widespread dust. While the SWIR spectrum of fine-grained soil (VBF-ZR-26) has a deeper feature at ~939 nm and similar strength at ~1400 nm, ~1900 nm, and ~2227 nm compared to other VBF-ZR targets (Fig. 2b), suggesting more pyroxene proportion in fine-grained soils. The SWIR spectrum of indurated soil (VBF-ZR-01) has a slightly weaker pyroxene feature and slightly stronger OH/H_2O bands, indicating a higher proportion of aluminosilicate.

We also compared the spectra of VBF-ZR targets to other phyllosilicates (nontronite, hectorite, chlorite, clinochlore, and montmorillonite) and gypsum from the U.S. Geological Survey (USGS) Spectral Library (Supplementary Fig. 5)[33], and found that
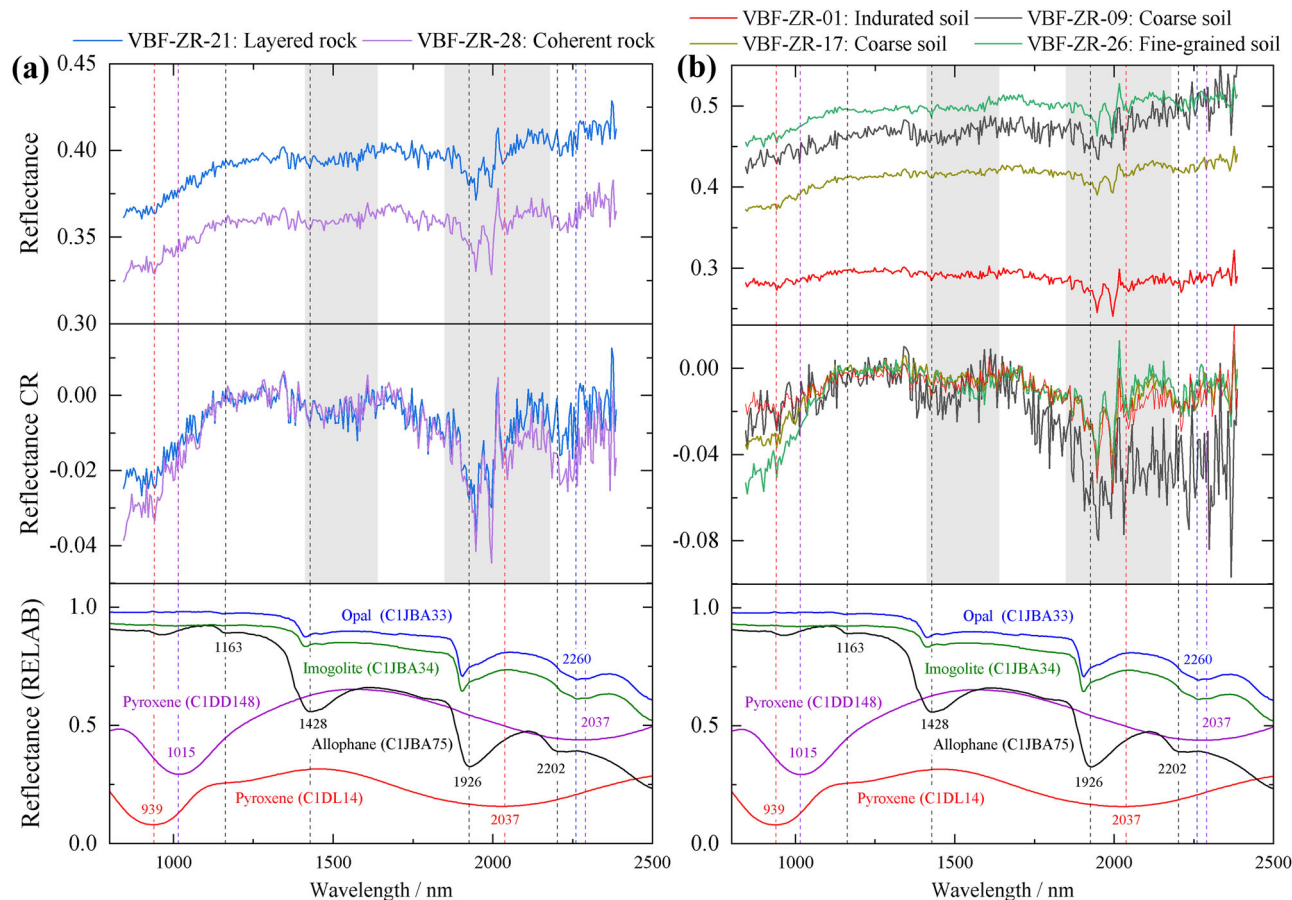
Fig. 2 Absolute SWIR spectra and mineral identification. The SWIR spectra before and after continuum removal (CR) of selected VBF-ZR rocks (**a**) and soils (**b**) compared to the spectra of pyroxene, imogolite, allophane, and opal from RELAB database. Dotted lines indicate the absorption centers of these phases. The gray regions indicate absorption features of the Martian atmosphere.

the spectra of these minerals are different to the SWIR spectra. In particular, the spectra of nontronite (No. SWa-1a and NG-1a) have a deep band at ~2295 nm, which is absent in SWIR spectra. The spectra of hectorite (No. SHCa-1), chlorite (No. SMR-13a), and clinochlore (No. GDS159) exhibit a feature at ~2300 nm, which is not observed in SWIR spectra. Montmorillonite spectrum (No. SWy-1) exhibits an obvious spectral feature at ~2204 nm consistent with the allophane spectrum (~2202 nm) but has a narrow band at ~1400 nm that is different from the broad H_2O bands in SWIR spectra. Gypsum spectrum (No. SU2202) has similar features to SWIR spectra including ~1400 nm and ~1900 nm bands, but exhibits an obvious feature at ~1747 nm and a convexity feature at ~2300 nm that are not observed in SWIR spectra. Overall, the distinct spectral features between VBF-ZR targets and these minerals suggest the absence or very few of these minerals in VBF rocks and soils.

In summary, the SWIR spectra of all VBF-ZR targets suggest mixtures of Fe, Ca-rich pyroxene with allophane and imogolite/ opal (at variable mixing ratios) in the soils covering the surface unit of the ZR landing site. Especially the layered rock and coherent rock have similar mineral types at the scale of SWIR (~69.4 mm and ~113.1 mm in diameter), which are composed of pyroxene and poorly-crystalline phases with absence or very few other secondary minerals, suggesting these two rocks may keep igneous nature after weak water-rock interaction.

Chemical compositions derived from LIBS spectral analysis. Each LIBS spectrum investigated here was averaged from 60 single laser shots on one target. The continuum background in these spectra was removed (Supplementary Fig. 6). Cluster analysis was firstly conducted by plotting the spectral line intensity ratio of $(Fe + Mg + Ca + Na + Al)/Ti$ vs. intensity ratio of Si/Ti from the normalized LIBS spectrum of each VBF-ZR target (details in Methods), together with the corresponding spectral line intensity ratios of seven silicate calibration targets (see Supplementary Notes 1)[25] carried by MarSCoDe (Fig. 3c), which can directly provide the qualitative classification of VBF-ZR targets.

Chemical compositions of VBF-ZR targets were derived from these LIBS spectra using a multivariate model, which was built using the relative intensities of 14 emission lines of nine major elements (Supplementary Table 3) in the normalized ChemCam laboratory spectra of 295 standards[34]. The performance of this multivariate model is evaluated by comparing the Root Mean Square Error (RMSE) values for eight major oxides (Supplementary Table 4) using four sets of LIBS spectra taken by different LIBS systems (details in Methods, Supplementary Fig. 7). The obtained similar RMSE values from different database support the suitableness of the developed multivariate model in this study. The proportion of dust in VBF-ZR soils (Supplementary Table 6) is assessed using compositions of indurated soil (VBF-ZR-01) and global average dust (using ChemCam results at Gale crater, Supplementary Table 7) as endmembers based on mass-balance analysis. Subsequently, we calculated the modal mineralogy using CIPW Norm Calculation (Supplementary Fig. 8 and Supplementary Table 8)[35]. It should be noted that CIPW does not take into account sedimentary processes.

The relative intensities of LIBS emission lines (Fig. 3a) and derived compositions (Fig. 3b) show the variation of major
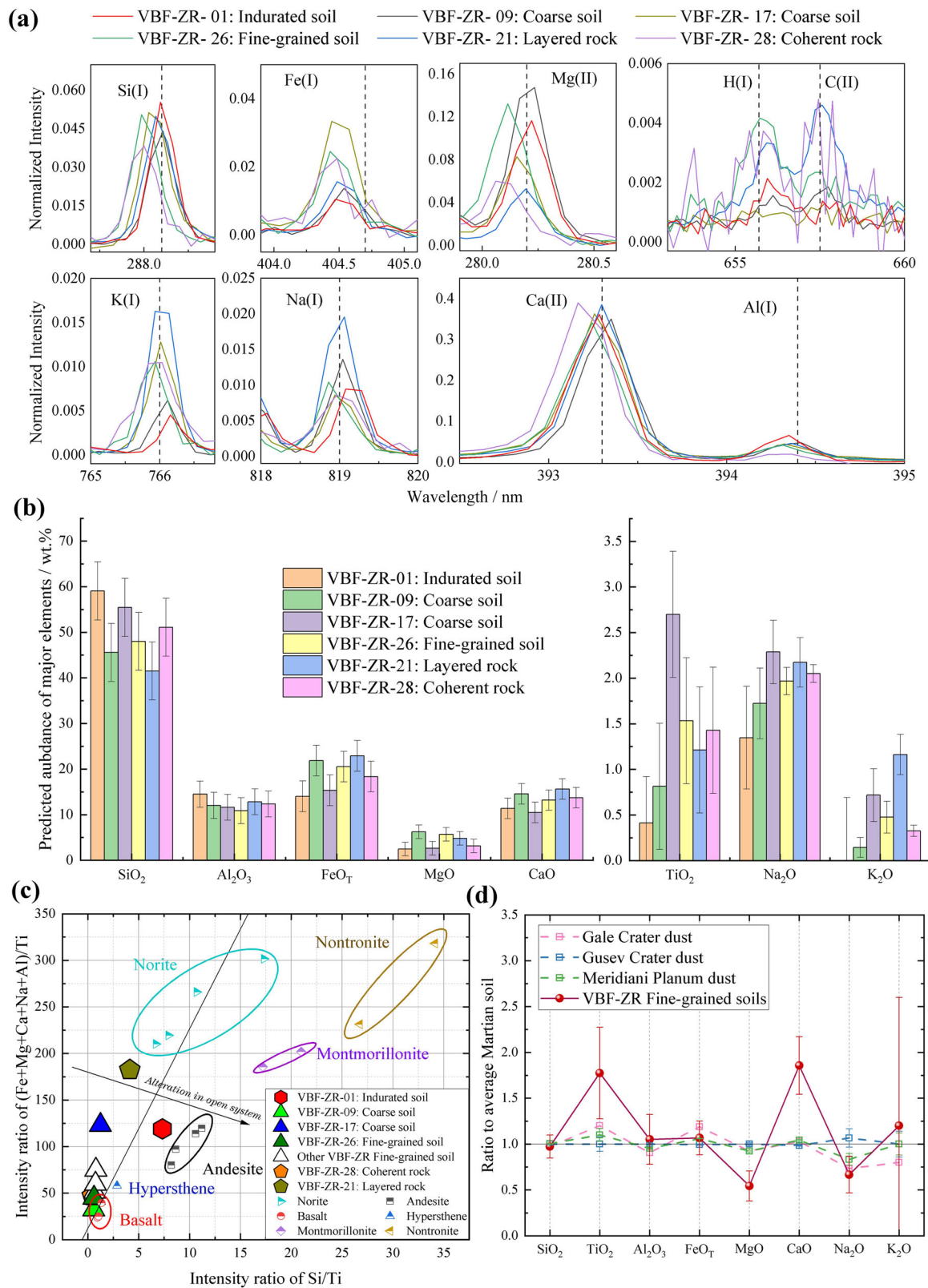
Fig. 3 LIBS spectra and chemical compositions of selected VBF-ZR targets. a Selected and normalized emission lines of Si, Fe, Mg, H, C, K, Na, Ca, and Al of six targets. **b** Major element concentrations in VBF-ZR targets, where the error bars are RMSEs of the multivariate model used in this study. **c** Cluster analysis using LIBS spectral line intensity ratios of the selected VBF-ZR targets and seven silicate cal-targets carried by MarSCoDe. The black line is a linear fit result using scatters of basalt, hypersthene, and norite cal-targets ($R^2 = 0.89$). **d** Relative concentrations of eight major elements at four landing sites normalized to the average Martian soil compositions (data in Supplementary Table 7). The error bars are the ratios between error values and average Martian soil compositions.
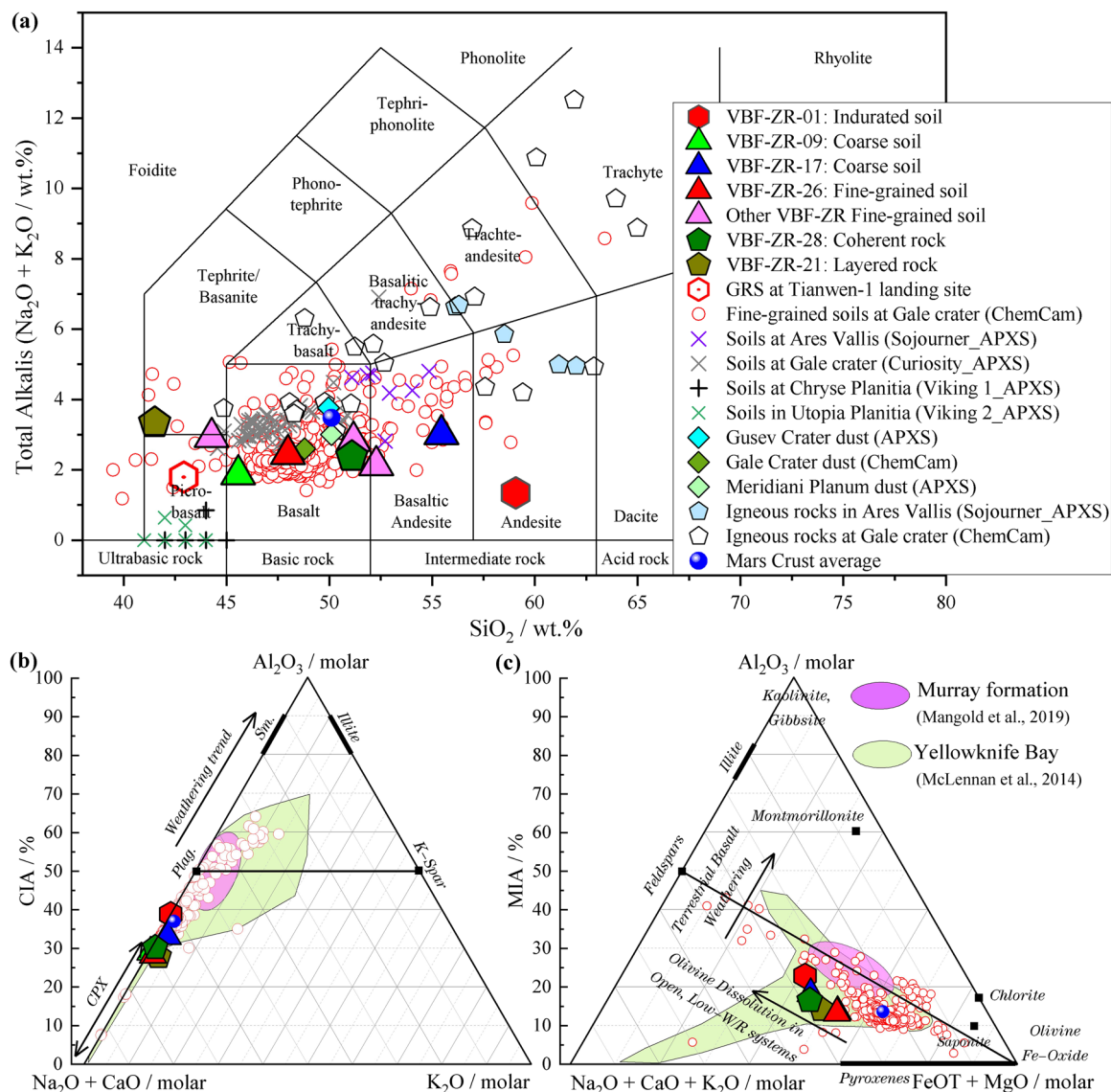
Fig. 4 Geochemical results of selected VBF-ZR targets. a Total alkalis (Na_2O and K_2O) vs. silica diagram of VBF-ZR targets that does not take into account sedimentary processes. Data of soils, dust, and rocks acquired by other missions are from Bridges et al.[75], Berger et al.[43], Lasue et al.[40], and Mangold et al.[55]. Compositions of fine-grained soils at Gale crater (red circle) are from PDS Geosciences Node at Washington University in St. Louis. **b, c** Ternary diagrams of Al_2O_3-($CaO+Na_2O$)-K_2O and Al_2O_3-($CaO+Na_2O+K_2O$)-(FeO_T+MgO), with CIA and MIA values on the vertical axis. ChemCam results from Murray formation and Yellowknife Bay in Gale crater are respectively from Mangold et al.[55] and McLennan et al.[53]. The average compositions of Mars crust are from Taylor et al.[51]. The big size of VBF-ZR data represents the currently used percent level (wt%) accuracy for them, which will be improved along with the Tianwen-1 mission development.

elements among the selected six VBF-ZR targets. Between the two rock targets, the coherent rock (VBF-ZR-28) has a mafic composition (Fig. 4a) with a relatively high concentration of SiO_2 (51 wt.%) and more pyroxene (~40%, Supplementary Fig. 8) than the layered rock (SiO_2 = 42 wt.%, pyroxene = ~25%) and occurs adjacent to the cluster of the basalt cal-targets (Fig. 3c). The layered rock (VBF-ZR-21) contains a higher concentration of mafic components (23 wt.% of FeO_T and 5 wt.% of MgO) than the coherent rock (18 wt.% of FeO_T and 3 wt.% of MgO). It occurs near the cluster of Fe-Mg-rich norite calibration targets in Fig. 3c, representing a mafic composition. Note that the H emission line (with good S/N) was observed in the LIBS spectrum of layered rock (Fig. 3a). All eight rocks exhibit Fe, Ca, Ti-rich (FeO_T = 22 ± 3 wt.%, CaO = 15 ± 1 wt.%, TiO_2 = 1.6 ± 0.3 wt.%) and Mg-deficit features (MgO = 5 ± 1 wt.%) compared to the Mars global dust. The Ca-rich compositions in these rocks are

consistent with the high-Ca pyroxene determined by their SWIR spectra. Most rocks (including the outcrop of VBF-ZR-21) have similar chemical compositions within the error of the multivariate model and similar mineral types although they are detected at different locations, suggesting they may reflect the local materials. Thus, the compositions of these rocks can reflect the special volcanism at the Tianwen-1 landing region.

For VBF-ZR soils, average compositions of soils can be characterized by multiple LIBS shots at one single point because the new portion of the soil will be ablated by the laser due to the disturbs of the shock wave caused by previous shots. The chemical compositions of soils are similar and the slight differences between them are within the RMSEs of the multivariate model in our work (6 wt.% of SiO_2, 3 wt.% of FeO_T, and 2 wt.% of MgO). The coarse soils at TAR1 (e.g., VBF-ZR-09) and fine-grained soils (e.g., VBF-ZR-26) at TAR3 have similar

compositions (e.g., 4–7 wt.% MgO and 18–24 wt.% FeO$_T$), which are adjacent to the cluster of basaltic cal-targets on MarSCoDe (Fig. 3c), suggesting that the coarse soils could be aggregates or precursor of fine particles[36,37]. The fine-grained soil (VBF-ZR-26) has a stronger H emission line (Fig. 3a) that can be assigned to adsorbed water[38] at grain surfaces and interstitial gaps. However, another coarse-grained soil (VBF-ZR-17) exhibits distinct compositions compared to fine-grained soils analyzed by the ZR rover, which has a higher SiO$_2$ (55 wt.% vs 44–52 wt.%), lower FeO$_T$ (15 wt.% vs 18–22 wt.%), and MgO (3 wt.% vs 4–6 wt.%; Fig. 3b and Supplementary Table 5). In cluster analysis, it lies in a zone that is distanced from the cluster of basalt, Fe-Mg-rich norite, and Si-rich andesite cal-targets (Fig. 3c). The slight difference in compositions of these three soils near different TARs may reflect their different proportions of silicic and mafic minerals at the submillimeter scale, suggesting their different mixing proportions of local materials and Mars global dust (22–75% in Supplementary Table 6) probably caused by sorting processes of aeolian sand along a transport pathway. This phenomenon is similar to the mixing effects of fine- and coarse-grained soils at Gale crater[36,37].

Interestingly, the indurated soil (VBF-ZR-01) has the strongest emission lines of Si and Al while relatively weak of Fe, K, and Na, indicating its distinct compositions from all other VBF-ZR targets. In cluster analysis (Fig. 3c), data from this target occur quite far from other VBF-ZR targets. It also has more SiO$_2$ (59 wt.%) and Al$_2$O$_3$ (15 wt.%) compared to other targets (SiO$_2$ < 55 wt.% and Al$_2$O$_3$ < 13 wt.%), which is consistent with more aluminosilicate in this target determined by SWIR spectra. In addition, the H emission line (S/N ~ 3) in its LIBS spectrum (Fig. 3a) also suggests the existence of H$_2$O/OH-bearing species in this dust-removed indurated soil. Compared to the basaltic indurated soil of the Rocknest Sand Shadow in Gale crater (CIA = ~33.4%)[39], the overall compositions of this target may be affected by chemical weathering. Considering the surface dust was removed from this target (by the turbulent airflow during landing), its distinct compositions may reflect the real compositional characteristics of local soils (beneath surface dust) at the Tianwen-1 landing site.

In addition, sulfur emission lines (e.g., S(II) at 543.0 nm, 545.5 nm, 548.0 nm, 553.8 nm, and 566.6 nm) are absent in the LIBS spectra of VBF-ZR targets (Supplementary Fig. 9). This may be due to the low response efficiency at the end wavelength region of MarSCoDe CCD (540–850 nm). It may be also caused by the average of 60 LIBS spectra at each point, which weakens the potential S lines. Thus, the sulfur in the detected targets may be lower than the limit of detection of MarSCoDe. This is consistent with the absence or very few sulfates in VBF-ZR targets determined using SWIR spectra.

Comparisons with GRS data and fine-grained soils at other landing sites. Two comparisons were made to evaluate the reliability of the above compositional measurements. Firstly, the chemistry of the fine-grained soil target (VBF-ZR-26) was compared with the finest fraction of soils and dust (1.4–2.5 μm) at other landing sites (Gale crater[40], Gusev crater[41], and Meridiani Planum[42]) on Mars that have similar compositions due to the global circulation of surface dust by regional and global dust storms[43–46]. It was found that VBF-ZR-26 (fine-grained soil) has a very similar composition to the average Martian surface soils, and the discrepancies are not very different between the VBF-ZR-26 target and the surface dust at the other three landing sites (Supplementary Table 7 and Fig. 3d). While the VBF-ZR-26 target has slightly higher CaO and lower MgO than dust, which may be contributed by the 23% Ca-rich and Mg-poor local

materials (e.g., the indurated soil has 11 wt.% CaO and 2 wt.% MgO in Supplementary Fig. 10) mixed with 73 % widespread dust (e.g., dust in Gale crater has 7.2 wt.% CaO and 8.5 wt.% MgO, shown in Supplementary Table 7). The mixture of local materials can also be reflected by the larger grain size of VBF-ZR fine-grained soils (~150 μm) than dust (1.4–2.5 μm). Secondly, an average of derived compositions of all VBF-ZR targets was compared with the published compositions (SiO$_2$, FeO$_T$, Na$_2$O, and K$_2$O) acquired by Mars Odyssey's Gamma-Ray Spectrometer (GRS)[47] at the Tianwen-1 landing site (Supplementary Table 9). In this limited comparison, the direct ratios of FeO$_T$/SiO$_2$ from both data sets are almost the same (0.43 for MarSCoDe and 0.41 for GRS), although the range of ZR rover observations is <2 km while the GRS data were extracted from a region of 5° × 5° (~300 km at the equator)[47].

The two comparisons above show that the quantitative compositional information of VBF-ZR targets can be extracted using the multivariate model developed in this study, and can be compared with the chemical compositions of widespread dust and fine-grained soils from other rover missions at different landing sites. The slightly distinct compositions of VBF-ZR targets compared to dust can reflect the Ca-rich and Mg-poor characteristics in local materials. Although at this early stage of the Tianwen-1 mission and different detection distances of VBF-ZR targets, we limit ourselves to the percent (wt%) level for compositional accuracy (Fig. 4a and Supplementary Table 5) for eight major oxides, that accuracy will be improved along with the mission development as more targets are analyzed.

Degree of chemical alteration. The degree of chemical alteration of VBF-ZR targets is characterized by the Chemical Index of Alteration (CIA) and the Mafic Index of Alteration (MIA). CIA is defined as the molar ratio of Al$_2$O$_3$ and the total of Al$_2$O$_3$, Na$_2$O, K$_2$O, and CaO[48], reflecting the release of Ca, Na, and K relative to Al. MIA is used to characterize the loss of Mg and Fe from mafic minerals in a reducing environment[49]. CIA and MIA can be integrated into Al$_2$O$_3$-(CaO+Na$_2$O)-K$_2$O and Al$_2$O$_3$-(CaO+Na$_2$O+K$_2$O)-(FeO$_T$+MgO) diagrams derived from LIBS spectral analyses (Fig. 4c, d).

In general, igneous rocks with a low degree of alteration have low CIA values. For instance, igneous rocks at Gale crater and Ares Vallis (in VBF) respectively have CIA values of 41.7 ± 6.3% (using ChemCam data[50]) and 37.4 ± 3.5 % (using APXS data[24]). In addition, the estimated Martian crust compositions also have a low CIA value of ~36.9% (using APXS data[51,52]). For comparison, the CIA values of Martian dust are measured around 36–37% at Gale crater[40], Gusev crater[41], and Meridiani Planum[42]. While the sediments from chemical weathering of mafic materials in open systems have higher CIA values than the parent rock (~40–45%, even ~50–55%)[53,54], and this trend from chemical weathering can be recognized in ternary diagrams (e.g., black arrows in Fig. 4b, c). For example, some altered materials at Yellowknife Bay at Gale crater exhibit extremely high CIA values (<70% based on ChemCam data, a green-colored patch in Fig. 4b)[53]. Most Murray formation rocks in Gale crater with substantial alteration also exhibit high CIA values of >45%[55] (a pink-colored patch in Fig. 4b). However, sedimentary materials with a high abundance of alkaline components (e.g., K-feldspar) would exhibit low CIA values similar to the CIA values of igneous rocks, which could not affect the CIA values of VBF-ZR targets due to their low abundance of alkaline components (2–3 wt% of Na$_2$O + K$_2$O). VBF-ZR rocks have low CIA values of 28% ± 8% (the layered rock) and 30% ± 8% (coherent rock), suggesting a small amount of amorphous aluminosilicates mixed with high-Ca pyroxene and thus these rocks may be igneous rocks with a low degree of

alteration and long-termed erosion of wind. Alternatively, low CIA values can be contributed by the local Ca-rich materials mixed with Mars global dust (CIA = ~36%).

Specifically, the VBF-ZR-01 target has the highest CIA value of 39% ± 9% as well as high SiO_2 and Al_2O_3 concentrations, which is consistent with its SWIR spectrum, and shows a higher portion of allophane and imogolite mixed with mafic materials due to the dust removal by the turbulent airflow during landing. Moreover, the VBF-ZR-01 target occurs at the upper end of a distribution line of VBF-ZR targets along the weathering trend (Fig. 4b, c) defined by Hurowitz et al.[56] and Ehlmann et al.[57], which is consistent with the results that VBF-ZR-01 contains more incipient weathering products based on its LIBS and SWIR spectra. With the surface dust being removed, this target can generally represent the local soils, a mixture of aluminosilicates and igneous parent materials or dust.

Discussion

The VBF was previously proposed to be formed from the sedimentary deposits in a standing body of water either from an Upper Hesperian ocean[6,10,13,14], outflow channels[5,16], or compaction and drainage activities[17,18], which experienced subsurface ice-related processes[1,4,19,20] and was covered by globally homogenized Mars surface dust. Based on SWIR analyses, the VBF-ZR targets are composed of amorphous aluminosilicates (allophane and imogolite/opal) and High-Ca pyroxene that are widely distributed in soils and rocks along the traverse path of the ZR rover. Most materials at the Tianwen-1 landing site have very low CIA values based on their LIBS spectra, also suggesting a mixture of local basaltic materials (e.g., VBF-ZR-09 and VBF-ZR-26) and Martian surface dust[41,43,51]. In addition, the indurated soil (VBF-ZR-01) target with the dust removal by the turbulent airflow during landing may represent the intrinsic VBF soils broadly distributed in the Tianwen-1 landing site, which has the highest CIA (39% ± 9%) with high Al_2O_3 abundance and the most amorphous aluminosilicates among all VBF-ZR targets.

Terrestrial allophane and imogolite are mainly associated with highly leached and weathered volcanic materials, which are characteristic of soils formed from the rapid weathering of volcanic glass in cold and low W/R systems[31,58–60] or in cold and icy terrains[61]. The release of Ca and Mg cations from basaltic glass can provide neutral to slightly acidic conditions (pH = 5–7) for allophane and imogolite formation[60,62,63]. Some allophane can also be precipitated from soil water (e.g., stream-deposits from a river in Japan[64]) with silica and hydroxy-Al ion[65]. On Mars, the allophane and imogolite have been identified at Mawrth Vallis, and were proposed to be generated from limited aqueous alteration of basaltic glass from rainy environment or melting snow/ice[63]. Based on those, we suggest that the amorphous aluminosilicates along the traverse path of the ZR rover are probably generated from the dissolution of basaltic glasses in an open system with a low W/R condition at low temperature. Alternatively, these aluminosilicates are precipitated from the soil solution with high silica and hydroxy-Al ion. Moreover, the absence of large amounts of other phyllosilicates (e.g., montmorillonite and nontronite) and sulfates also suggests a limited water-rock interaction which may be generated from limited water or short-term soil solution.

Overall, in-situ observations of ZR rover suggest that VBF-ZR materials still keep the igneous nature with limited alteration features, and the products are then suffered a long-time wind aeolian erosion leading to mixing and sorting along a transport pathway. The geochemistry and mineralogy of local rocks and soils support that the Tianwen-1 landing site (to the depth that ZR rover can measure) within VBF may have the deposits generated by chemical weathering from extensive volcaniclastic soils by limited water (e.g., rainy or melting from frost/snow/ice) or from a short-lived standing body of water (e.g., melting of glaciers or sourced from southern highlands). In terms of the four hypotheses of the VBF origin, our study suggests that the limited water interaction under cold conditions at the Tianwen-1 landing site mostly supports the hypotheses relating to the ephemeral frozen ocean and sublimation.

Methods

SWIR spectra processing. Mineralogy information of VBF-ZR materials can be investigated using SWIR spectra. The original radiance data acquired by SWIR are converted to reflectance after wavelength calibration, and continuum spectra are subsequently deducted to highlight absorption features. The processing steps of SWIR spectra are as follows.

1) Wavelength calibration. The wavelength shift of SWIR spectra is determined using the absorption features of the Martian atmosphere. The SWIR spectra of VBF-ZR are firstly converted into reflectance by dividing the solar spectrum provided by Gueymard[66], and absorption centers are identified and compared to the features provided by CRISM (Compact Reconnaissance Imaging Spectrometer for Mars) Analysis Toolkit (CAT)[32] (Supplementary Table 2). We find SWIR spectra shift ~10 nm to a longer wavelength than CRISM spectra (Supplementary Fig. 2a), which is subsequently corrected (Supplementary Fig. 2b).

2) Transition into absolute reflectance. The SWIR radiance spectra are converted to absolute reflectance using Exp.1. Relative reflectance spectra of VBF-ZR targets are acquired from their radiance spectra divided by the radiance of two calibration targets (white and gray pieces), with the hypothesis that calibration targets are total reflectors. Subsequently, the relative reflectance data are converted to absolute reflectance by multiplying the absolute reflectance of SWIR calibration targets (Supplementary Fig. 3). The pre-processing of SWIR spectra can reduce the effects of the absorption features of Martian atmosphere.

$$R_{SWIR}(Absolute\ reflectance) = \frac{I_{SWIR}}{I_{SWIRC}} R_{SWIRC}(Absolute\ reflectance) \quad (1)$$

where I_{SWIR} and I_{SWIRC} are radiance data of VBF-ZR targets and two calibration targets (white and gray pieces) collected by SWIR spectrometer. R_{SWIRC} represents the absolute reflectance of calibration targets given in Supplementary Fig. 3.

3) Continuum removal. The continuum removal of SWIR spectra is conducted to highlight the spectral absorption features (Supplementary Fig. 11). The continuum is defined as a polyline using four tie points at ~1187 nm, ~1251 nm, ~1653 nm, and ~2236 nm. The linear continuum at a lower wavelength than the first tie points (~1187 nm) is defined as an extended line of the straight line between the first(at ~1187 nm) and the second tie points (at ~1251 nm).

LIBS spectra processing. The chemical composition of a target can be derived from the emission lines in its LIBS spectrum, which was averaged from 60 spectra of 60 single laser shots. In this study, a multivariate model is built using the intensities of selected emission lines in the ChemCam LIBS database collected in the laboratory. The model is applied to interpret the LIBS spectra collected using a LIBS system at Shandong University, China (SDU-LIBS) to verify the applicability of the model among different LIBS systems and the uncertainties. Finally, the chemical compositions of VBF-ZR targets are derived using this model. The RMSEs of these different LIBS databases were compared. The processing of VBF-ZR-LIBS spectra has the following steps.

1) Continuum removal. The emission lines in LIBS spectra are affected by background continuum emission caused by bremsstrahlung and ion-electron recombination processes[34,67]. The continuum background spectra are obtained by the interpolation of local minima using the spline function and are subtracted from the LIBS spectra. The instrument white noise spectra are not considered due to the reduced effects of instrumental noise in terms of the averaging of 60 LIBS spectra from a single target. The LIBS spectrum before and after continuum removal is provided in Supplementary Fig. 6.

2) Identification of the emission lines. The 14 emission lines of major elements (Si, Ti, Al, Fe, Mg, Ca, Na, K, H, C, and O) are identified and selected according to the NIST database[68] (Supplementary Table 3). Those emission lines have high-intensity values and do not overlap with other lines (as shown in Supplementary Fig. 12). For elements with multiple lines (Fe, Mg, Ca, Al, Na), two independent and strong emission lines are selected. Only one strong emission line is selected for Ti due to its low abundance in most rocks and soils. For Si, only the neutral emission peak at ~288.3 nm has a high intensity and is not affected by the emission lines of Fe. Only one emission line is selected for K and O at ~766.7 nm and ~777.6 nm, respectively, because no other strong emission lines can be seen as candidates. A summary list of selected emission lines is shown in Supplementary Table 3. Moreover, obvious self-absorption is not observed in all selected emission lines, which may be due to the low atmospheric pressure on Mars[69,70].

3) Cluster analysis of VBF-ZR targets and cal-targets. Cluster analysis was conducted by plotting the spectral line intensity ratio of (Fe + Mg+Ca+Na+Al)/Ti vs. the line intensity ratio of Si/Ti from the normalized LIBS spectra of VBF-ZR

targets and cal-targets (andesite, hypersthene, basalt, norite, montmorillonite, and nontronite). These intensity ratios correspond to the chemical space of (olivine + plagioclase + clinopyroxene)/Ti vs Si/Ti, which defines a 1:1 basalt line and a direction of chemical weathering according to igneous fractionation and crystal sorting in magmatic systems[71].

Multivariate model using ChemCam LIBS database. The ChemCam LIBS database of 295 standards is selected to build a multivariate model and interpret the LIBS spectra acquired by MarSCoDe. Those ChemCam LIBS spectra are acquired using the ChemCam engineering model at a 1.5 m standoff distance. LIBS spectra are acquired at five different spots on each sample with 50 laser shots at each location, and 250 spectra are obtained and averaged for each sample[34]. The steps to build our multivariate model are as follows.

1) Selection of ChemCam database. The ChemCam standards are composed of igneous, sedimentary, and metasedimentary samples as well as some doped mixtures. Some types of these samples (e.g., sulfates and chloride) are not observed at the Tianwen-1 landing site, and hence not selected. In addition, we did not select the samples with the total oxide abundance of eight major elements (SiO_2, TiO_2, FeO_T, MgO, Al_2O_3, CaO, Na_2O, K_2O) larger than 110 wt.% and lower than 90 wt.%. Subsequently, the compositions of the 295 selected samples are normalized to the total oxide abundance of 8 major elements. Finally, the LIBS spectra of these ChemCam standards are adopted in our model.

2) Earth-to-Mars correction. LIBS spectra are different in terrestrial laboratories and on Mars due to different plasma temperatures achieved by the flight model (FM) laser on Mars and in the laboratory. The Earth-to-Mars correction is performed to compensate for these spectral differences. The selected LIBS spectra are multiplied by the pixel-by-pixel correction factors developed by the LIBS spectra of ChemCam Calibration Targets (CCCT) obtained on Mars and in the laboratory[34].

3) Normalization of the emission lines' intensity. Normalization was conducted using the total intensity of selected emission lines of each sample. Subsequently, the intensities of elements with multiple emission lines (e.g., Fe405 and Fe438) are summed. Finally, nine intensities for nine major elements (Si, Ti, Fe, Mg, Al, Ca, Na, K, and O) are acquired for each sample.

4) Build a multivariate model. The normalized emission intensities for nine major elements are used to build a multivariate model using a polynomial fitting algorithm to predict the oxide abundance of eight major oxides (SiO_2, TiO_2, FeO_T, MgO, Al_2O_3, CaO, Na_2O, and K_2O). Polynomial fitting is selected with the intent to reduce the disturbance effects in LIBS intensities between elements (i.e., chemical matrix effects). The performance of this model is determined by RMSE between actual and derived compositions as follows.

$$RMSE = \sqrt{\frac{1}{n}\sum_{i=1}^{n}(y_{ip} - y_i)^2} \qquad (2)$$

where n is the number of samples, y_i and y_{ip} are actual and derived compositions.

Deriving compositions of VBF-ZR targets. (1) Response transformation from MarSCoDe to ChemCam

In order to properly extract chemical compositions of the VBF-ZR targets based on the ZR-LIBS spectra using the model that we built using the ChemCam database, the response difference between these two LIBS systems should be removed. First, the radiance calibration methods and the units of LIBS intensity are different for ZR-LIBS and ChemCam. The system response values of ChemCam (Digital Number, DN) are converted into radiance in photons·s^{-1} cm^{-1} sr^{-1} µm^{-1}[167,72]. While the unit of ZR-LIBS radiance is W·m^{-2} sr^{-1} nm^{-1}[125], which is converted into photons·s^{-1} cm^{-1} sr^{-1} µm^{-1} by dividing the photon energy as follows.

$$I_{ChemCam}(photons) = \frac{I_{MarSCoDe}(W)}{E} \qquad (3)$$

where $I_{ChemCam}$ and $I_{MarSCoDe}$ respectively represent the LIBS intensities of ChemCam and MarSCoDe. E indicates the photon energy, which can be expressed as[73]

$$E = \frac{hc}{\lambda} \qquad (4)$$

where h is the Planck constant, c is the speed of light, and λ is the wavelength.

Therefore, the response transformation can be expressed as

$$I_{MarSCoDe}(photons) = \frac{I_{MarSCoDe}(W)\lambda}{hc} \qquad (5)$$

(2) Intensity transformation using LIBS spectra of a norite cal-target

The norite sample is the only on-board calibration target carried by both ChemCam and MarSCoDe (Supplementary Table 10)[25], and its compositions are provided by Clegg et al.[34]. Thus, the LIBS spectral intensities of this sample can be used for cross-calibration between these two flight LIBS systems. The same set of 14 emission lines in norite spectra (both ZR-LIBS and ChemCam) is obtained and normalized using the same method for the 295 spectra of the ChemCam LIBS database. The different intensity values of emission lines between ZR-LIBS and ChemCam (Supplementary Fig. 13a) may be due to the different radiance

calibration methods of these two LIBS systems[25,72]. Specifically, solid angle and imaged source area of the MarSCoDe telescope are not considered in ZR-LIBS radiance calibration, while these parameters are constant for all bands in each ZR-LIBS spectrum and can be removed in normalization.

The ratios between ChemCam and MarSCoDe intensities (Supplementary Fig. 13b) are used to further transform from MarSCoDe to ChemCam response. This type of transfer method has been applied in the Earth-to-Mars correction of ChemCam and SuperCam[34,74]. The intensity ratio of Ti(I) line at ~335.5 nm is larger than the values of other elements, which is ~10 times higher than the ratio of Na(I) line at ~819.1 nm. This variation may be due to different laser irradiance on targets (~6.4 GW cm^{-2} of MarSCoDe[25], ~3.1 GW cm^{-2} of ChemCam[72]), which can be reduced by intensity transformation from MarSCoDe to ChemCam as follows.

$$I_{ChemCam}(photons) = I_{MarSCoDe}(photons)\frac{I_{ChemCam\_norite}}{I_{MarSCoDe\_norite}} \qquad (6)$$

where $I_{ChemCam\_norite}$ and $I_{MarSCoDe\_norite}$ are the intensity values of selected emission lines from the ChemCam and MarSCoDe-LIBS spectra of norite cal-target, respectively.

3) Deriving compositions of VBF-ZR targets

Similar to ChemCam data processing, nine normalized spectral intensities for nine elements are extracted from each ZR-LIBS spectrum and are used to derive the abundance for oxides of eight major elements (SiO_2, TiO_2, FeO_T, MgO, Al_2O_3, CaO, Na_2O, and K_2O) of VBF-ZR targets using the multivariate model that we built.

Validation of the multivariate model. It is critical to evaluate whether the multivariate model that we built using the ChemCam spectral database is applicable for ZR-LIBS compositional extraction. The results of this evaluation are shown in Supplementary Fig. 7.

Our multivariate model is firstly applied to the laboratory LIBS spectra of 295 ChemCam standards, and the ChemCam spectra of seven ChemCam Calibration Targets (CCCT). In Supplementary Fig. 7a, b, the actual compositions of these samples and the derived compositions (in wt.%) using our multivariate model are shown along a 1:1 line. We noticed that ~92% of 295 ChemCam standards and all data from CCCT fall into a buffer zone of ±10 wt.%. Supplementary Table 4 lists the RMSEs using our multivariate model (e.g., 6.3 wt.% and 6.0 wt.% for SiO_2 in 295 ChemCam standards and CCCT) are comparable to the published values by ChemCam and SuperCam teams (i.e., 5.3 wt.% and 6.1 wt.% for SiO_2 using ChemCam model[34] and SuperCam model[74]).

Secondly, our multivariate model is applied to the laboratory LIBS spectra of 168 SDU-LIBS standards collected using SDU-LIBS system (the other four samples are the same standards in 295 ChemCam standards used for LIBS system response transformation, Supplementary Notes 2), and also applied to the LIBS spectrum of the norite cal-target collected by ZR-LIBS system. Using the same methodology (as Supplementary Fig. 7a, b) to plot the actual and derived compositions in Supplementary Fig. 7c, d along a 1:1 line, we found that >72% data (but lower for FeO_T of ~43%) from 168 samples and all data from norite sample fall into a buffer zone of ±10 wt%. Similarly, comparable RMSEs (Supplementary Table 4) are obtained from those LIBS spectra of four different LIBS systems (e.g., 6.3 wt.%, 6.0 wt.%, 9.1 wt.%, and 7.4 wt.% for SiO_2 in 295 ChemCam standards, CCCT, 168 SDU-LIBS standards, and norite cal-target). Slightly higher RMSEs are obtained for the spectra in SDU-LIBS standards, due to the low Signal to Noise Ratio of the averaged spectra (30 spectra per sample vs. 250 spectra per sample in the ChemCam spectral database), especially for Fe405, and Na819 emission lines.

Overall, the comparable RMSEs (Supplementary Table 4) indicate that our multivariate model (with proper pre-processing) works well on the spectra from different LIBS systems, and accurate elemental compositions of VBF-ZR targets can be derived from ZR-LIBS spectra.

Data availability
The authors declare that the data supporting the findings of this study have been deposited in Figshare (https://figshare.com/articles/dataset/Communications-Earth-Envt-2022/21113962).

Code availability
Code for all analyses are available from the corresponding author on request.

References
1. Zhao, J. et al. Geological characteristics and targets of high scientific interest in the Zhurong landing region on Mars. *Geophys. Res. Lett.* **48**, e2021GL094903 (2021).

2. Wu, B. et al. Characterization of the candidate landing region for tianwen-1–China's first mission to mars. *Earth Space Sci.* **8**, e2021EA001670 (2021).

3. Wu, X. et al. Geological characteristics of China's Tianwen-1 landing site at Utopia Planitia, Mars. *Icarus* **370**, 114657 (2021).

4. Ye, B. et al. Geomorphologic exploration targets at the Zhurong landing site in the southern Utopia Planitia of Mars. *Earth Planet. Sci. Lett.* **576**, 117199 (2021).

5. Tanaka, K. L., Robbins, S., Fortezzo, C., Skinner, J. Jr & Hare, T. M. The digital global geologic map of Mars: Chronostratigraphic ages, topographic and crater morphologic characteristics, and updated resurfacing history. *Planet. Space Sci.* **95**, 11–24 (2014).

6. Kreslavsky, M. A. & Head, J. W. Fate of outflow channel effluents in the northern lowlands of Mars: The Vastitas Borealis Formation as a sublimation residue from frozen ponded bodies of water. *J. Geophys. Res.: Planets* **107**, 4-1-4-25 (2002).

7. Scott D. H., Tanaka K. L. *Geologic Map Of The Western Equatorial Region Of Mars* (U.S. Geological Survey, 1986).

8. Survey G., Greeley R., Guest J. *Geologic Map Of The Eastern Equatorial Region Of Mars* (U.S. Geological Survey, 1987).

9. Survey G., Tanaka K. L., Scott D. H. *Geologic Map Of The Polar Regions Of Mars* (U.S. Geological Survey, 1987).

10. Kreslavsky, M. A. & Head, J. W. III Kilometer-scale roughness of Mars: Results from MOLA data analysis. *J. Geophys. Res.: Planets* **105**, 26695–26711 (2000).

11. Parker, T. J., Gorsline, D. S., Saunders, R. S., Pieri, D. C. & Schneeberger, D. M. Coastal geomorphology of the Martian northern plains. *J. Geophys. Res.: Planets* **98**, 11061–11078 (1993).

12. Parker, T. J., Saunders, R. S. & Schneeberger, D. M. Transitional morphology in west Deuteronilus Mensae, Mars: Implications for modification of the lowland/upland boundary. *Icarus* **82**, 111–145 (1989).

13. Head J. W., Wilson L. *Volcano-Ice Interactions on Earth and Mars*, vol. 202, pp 27-57 (Geological Society, Special Publications, 2002).

14. Schmidt, F. et al. Circumpolar ocean stability on Mars 3 Gy ago. *Proc. Natl Acad. Sci. USA* **119**, e2112930118 (2022).

15. Golombek, M. et al. Overview of the Mars Pathfinder Mission: Launch through landing, surface operations, data sets, and science results. *J. Geophys. Res.: Planets* **104**, 8523–8553 (1999).

16. Tanaka, K. L. Geology and insolation-driven climatic history of Amazonian north polar materials on Mars. *Nature* **437**, 991–994 (2005).

17. Allen, C. C. et al. Fluid expulsion in terrestrial sedimentary basins: A process providing potential analogs for giant polygons and mounds in the martian lowlands. *Icarus* **224**, 424–432 (2013).

18. Salvatore, M. & Christensen, P. On the origin of the Vastitas Borealis formation in Chryse and Acidalia Planitiae, Mars. *J. Geophys. Res.: Planets* **119**, 2437–2456 (2014).

19. Levy, J. S., Fassett, C. I., Head, J. W., Schwartz, C. & Watters, J. L. Sequestered glacial ice contribution to the global Martian water budget: geometric constraints on the volume of remnant, midlatitude debris-covered glaciers. *J. Geophys. Res.: Planets* **119**, 2188–2196 (2014).

20. Boyce J. M., Mouginis-Mark P. & Garbeil H. Ancient oceans in the northern lowlands of Mars: Evidence from impact crater depth/diameter relationships. *J. Geophys. Res.: Planets* **110**, E03008 (2005).

21. Stuurman, C. et al. SHARAD detection and characterization of subsurface water ice deposits in Utopia Planitia, Mars. *Geophys. Res. Lett.* **43**, 9484–9491 (2016).

22. Feldman, W. C. et al. Vertical distribution of hydrogen at high northern latitudes on Mars: The Mars Odyssey Neutron Spectrometer. *Geophys. Res. Lett.* **34**, L05201 (2007).

23. Toulmin, I. I. I. P. et al. Geochemical and mineralogical interpretation of the Viking inorganic chemical results. *J. Geophys. Res.* **82**, 4625–4634 (1977).

24. Foley, C. N., Economou, T. & Clayton, R. N. Final chemical results from the Mars Pathfinder alpha proton X-ray spectrometer. *J. Geophys. Res.: Planets* **108**, 8096 (2003).

25. Xu, W. et al. The MarSCoDe instrument suite on the mars rover of China's tianwen-1 mission. *Space Sci. Rev.* **217**, 1–58. (2021).

26. Jiang, X., Yang, B. & Li, S. Overview of China's 2020 Mars mission design and navigation. *Astrodynamics* **2**, 1–11 (2018).

27. Zou, Y. et al. Scientific objectives and payloads of Tianwen-1, China's first Mars exploration mission. *Adv. Space Res.* **67**, 812–823 (2021).

28. Balme, M., Berman, D. C., Bourke, M. C. & Zimbelman, J. R. Transverse aeolian ridges (TARs) on Mars. *Geomorphology* **101**, 703–720 (2008).

29. Berman, D. C., Balme, M. R., Michalski, J. R., Clark, S. C. & Joseph, E. C. High-resolution investigations of transverse aeolian ridges on Mars. *Icarus* **312**, 247–266 (2018).

30. Sherman, D. M. & Vergo, N. Optical (diffuse reflectance) and Mössbauer spectroscopic study of nontronite and related Fe-bearing smectites. *Am. Mineral.* **73**, 1346–1354 (1988).

31. Bishop, J. L. et al. Spectral and hydration properties of allophane and imogolite. *Clays Clay Miner.* **61**, 57–74 (2013).

32. Viviano-Beck, C. E. et al. Revised CRISM spectral parameters and summary products based on the currently detected mineral diversity on Mars. *J. Geophys. Res.: Planets* **119**, 1403–1431 (2014).

33. Clark, R. N. et al. USGS digital spectral library splib06a. Report No.: 2327-638X (US Geological Survey, 2007).

34. Clegg, S. M. et al. Recalibration of the Mars Science Laboratory ChemCam instrument with an expanded geochemical database. *Spectrochim. Acta B-At. Spectrosc.* **129**, 64–85 (2017).

35. Hollocher, K. *CIPW Norm Calculation Program* (Geology Department, Union College, 2004).

36. Meslin, P.-Y. et al. Soil diversity and hydration as observed by ChemCam at Gale Crater, Mars. *Science* **341**, 1238670 (2013).

37. Cousin, A. et al. Compositions of coarse and fine particles in martian soils at gale: A window into the production of soils. *Icarus* **249**, 22–42 (2015).

38. Meslin, P.-Y. et al. Soil diversity and hydration as observed by ChemCam at Gale Crater, Mars. *Science* **341**, 1238670 (2013).

39. Blake, D. F. et al. Curiosity at Gale crater, Mars: characterization and analysis of the Rocknest sand shadow. *Science* **341**, 1239505 (2013).

40. Lasue, J. et al. Martian eolian dust probed by ChemCam. *Geophys. Res. Lett.* **45**, 10,968–910,977. (2018).

41. Gellert, R. et al. Alpha Particle X-ray Spectrometer (APXS): results from Gusev crater and calibration report. *J. Geophys. Res.: Planets* **111**, E02S05 (2016).

42. Morris, R. V. et al. Mössbauer mineralogy of rock, soil, and dust at Meridiani Planum, Mars: Opportunity's journey across sulfate-rich outcrop, basaltic sand and dust, and hematite lag deposits. *J. Geophys. Res.: Planets* **111**, E12S15 (2006).

43. Berger, J. A. et al. A global Mars dust composition refined by the Alpha-Particle X-ray Spectrometer in Gale Crater. *Geophys. Res. Lett.* **43**, 67–75 (2016).

44. McGlynn I. O., Fedo C. M. & McSween Jr H. Y. Origin of basaltic soils at Gusev crater, Mars, by aeolian modification of impact-generated sediment. *J. Geophys. Res.: Planets* **116**, E00F22 (2011).

45. McSween, H. Y. & Keil, K. Mixing relationships in the Martian regolith and the composition of globally homogeneous dust. *Geochim. Cosmochim. Acta* **64**, 2155–2166 (2000).

46. Clancy R. T., Wolff M. J. & Christensen P. R. Mars aerosol studies with the MGS TES emission phase function observations: Optical depths, particle sizes, and ice cloud types versus latitude and solar longitude. *J. Geophys. Res.: Planets* **108**, E9,5098 (2003).

47. Boynton, W. et al. Concentration of H, Si, Cl, K, Fe, and Th in the low-and mid-latitude regions of Mars. *J. Geophys. Res.: Planets* **112**, E12S99 (2007).

48. Nesbitt, H. & Young, G. Early Proterozoic climates and plate motions inferred from major element chemistry of lutites. *Nature* **299**, 715–717 (1982).

49. Babechuk, M., Widdowson, M. & Kamber, B. Quantifying chemical weathering intensity and trace element release from two contrasting basalt profiles, Deccan Traps, India. *Chem. Geol.* **363**, 56–75 (2014).

50. Filiberto, J. Geochemistry of Martian basalts with constraints on magma genesis. *Chem. Geol.* **466**, 1–14 (2017).

51. Taylor S. R. & McLennan S. *Planetary Crusts: Their Composition, Origin And Evolution*, Vol. 10 (Cambridge University Press, 2009).

52. Hahn B. C. & McLennan S. M. Evolution and geochemistry of the Martian crust: integrating mission. *7th International Conference On Mars*. Pasadena. p. 3179.

53. McLennan, S. M. et al. Elemental geochemistry of sedimentary rocks at yellowknife bay, Gale Crater, Mars. *Science* **343**, 1244734 (2014).

54. Nesbitt H. W. in *Geochemistry of Sediments and Sedimentary Rocks*, Vol. 4, p. 39–51 (Geological Association of Canada, 2003).

55. Mangold, N. et al. Chemical alteration of fine-grained sedimentary rocks at Gale crater. *Icarus* **321**, 619–631 (2019).

56. Hurowitz, J. A. & McLennan, S. M. A~ 3.5 Ga record of water-limited, acidic weathering conditions on Mars. *Earth Planet. Sci. Lett.* **260**, 432–443 (2007).

57. Ehlmann, B. L. et al. Subsurface water and clay mineral formation during the early history of Mars. *Nature* **479**, 53–60 (2011).

58. Parfitt, R. L. & Hemni, T. Structure of some allophanes from New Zealand. *Clays Clay Miner.* **28**, 285–294 (1980).

59. Bishop, J. L. et al. Surface clay formation during short-term warmer and wetter conditions on a largely cold ancient Mars. *Nat. Astron.* **2**, 206–213 (2018).

60. Arnalds, O. The influence of volcanic tephra (ash) on ecosystems. *Adv. Agron.* **121**, 331–380 (2013).

61. Rampe, E. et al. A mineralogical study of glacial flour from Three Sisters, Oregon: An analog for a cold and icy early Mars. *Earth Planet. Sci. Lett.* **584**, 117471 (2022).

62. Dahlgren, R., Saigusa, M. & Ugolini, F. The nature, properties and management of volcanic soils. *Adv. Agron.* **82**, 113–182 (2004).

63. Bishop, J. L. & Rampe, E. B. Evidence for a changing Martian climate from the mineralogy at Mawrth Vallis. *Earth Planet. Sci. Lett.* **448**, 42–48 (2016).

64. Inoue, K. & Yoshida, M. The occurrence of allophane in stream-deposits from Shishigahana at the northern foot of Mt. Chokai, Japan. *Clay Sci.* **5**, 267–276 (1980).

65. Harsh, J., Chorover, J. & Nizeyimana, E. Allophane and imogolite. *Soil Mineral. Environ. Appl.* **7**, 291–322 (2002).

66. Gueymard, C. A. The sun's total and spectral irradiance for solar energy applications and solar radiation models. *Solar Energy* **76**, 423–453 (2004).

67. Wiens, R. C. et al. Pre-flight calibration and initial data processing for the Chem Cam laser-induced breakdown spectroscopy instrument on the Mars Science Laboratory rover. *Spectrochim. Acta Part B-At. Spectrosc.* **82**, 1–27 (2013).

68. Kramida A., Ralchenko Y. & Reader J. (2020) NAT. *NIST Atomic Spectra Database (ver. 5.8)* (National Institute of Standards and Technology, 2021).

69. Cousin, A. et al. Laser induced breakdown spectroscopy library for the Martian environment. *Spectrochim. Acta Part B-At. Spectrosc.* **66**, 805–814 (2011).

70. Fabre, C. et al. In situ calibration using univariate analyses based on the onboard ChemCam targets: first prediction of Martian rock and soil compositions. *Spectrochim. Acta Part B-At. Spectrosc.* **99**, 34–51 (2014).

71. Berger, J. A. et al. Elemental composition and chemical evolution of geologic materials in Gale Crater, Mars: APXS results from Bradbury landing to the Vera Rubin ridge. *J. Geophys. Res.: Planets* **125**, e2020JE006536 (2020).

72. Wiens, R. C. et al. The ChemCam instrument suite on the Mars Science Laboratory (MSL) rover: Body unit and combined system tests. *Space Sci. Rev.* **170**, 167–227 (2012).

73. Einstein, A. Generation and conversion of light with regard to a heuristic point of view. *Ann. Phys.* **17**, 132–148 (1905).

74. Anderson, R. B. et al. Post-landing major element quantification using SuperCam laser induced breakdown spectroscopy. *Spectrochim. Acta Part B: At. Spectrosc.* **188**, 106347 (2021).

75. Bridges, N. T., Crisp, J. A. & Bell, J. F. III Characteristics of the Pathfinder APXS sites: implications for the composition of Martian rocks and soils. *J. Geophys. Res.: Planets* **106**, 14621–14665 (2001).

Acknowledgements

Author contributions

Z.C.L. designed the research. C.Q.L. and Z.C.L. performed the research. E.B.S., H.J.C., X.H.F., L.Q., J.C., and J.Z.L. also contributed to the geological interpretations. Z.C.W., J.Z., P.L., Y.Q.X., L.Z., and H.C.B. assisted with the processing of the MarSCoDe LIBS spectra. S.K.T. and E.B.S. helped to characterize mineralogy using SWIR spectra. B.L., S.W., and S.K.T. helped to produce the camera data. We thank the team of the Tianwen-1 Project for their valuable and efficient assistance with providing the data and data calibration.

Competing interests

The authors declare no competing interests.

Additional information

Supplementary information The online version contains supplementary material available at https://doi.org/10.1038/s43247-022-00614-3.

Correspondence and requests for materials should be addressed to Zongcheng Ling.

Peer review information *Communications Earth & Environment* thanks Elizabeth Rampe, Candice Bedford and William Rapin for their contribution to the peer review of this work. Primary Handling Editors: Claire Nichols, Joe Aslin, Clare Davis.

Reprints and permission information is available at http://www.nature.com/reprints

Publisher's note Springer Nature remains neutral with regard to jurisdictional claims in published maps and institutional affiliations.